Received: 31 July 2023 | Revised: 3 October 2023 | Accepted: 9 October 2023

DOI: 10.1002/mp.16804

RESEARCH ARTICLE

MEDICAL PHYSICS

Robust stochastic optimization of needle configurations for robotic HDR prostate brachytherapy

Stefan Gerlach[1] | **Frank-André Siebert**[2] | **Alexander Schlaefer**[1]

[1]Institute of Medical Technology and Intelligent Systems, Hamburg University of Technology, Hamburg, Germany

[2]Department of Radiation Oncology, Karl-Lennert-Krebscentrum Nord, University Medical Center Schleswig-Holstein, Campus Kiel, Kiel, Germany

Correspondence
Stefan Gerlach, Institute of Medical Technology and Intelligent Systems, Hamburg University of Technology, Hamburg, Germany.
Email: stefan.gerlach@tuhh.de

Funding information
Deutsche Forschungsgemeinschaft, Grant/Award Number: 1844/6-1

Abstract

Background: Ideally, inverse planning for HDR brachytherapy (BT) should include the pose of the needles which define the trajectory of the source. This would be particularly interesting when considering the additional freedom and accuracy in needle pose which robotic needle placement enables. However, needle insertion typically leads to tissue deformation, resulting in uncertainty regarding the actual pose of the needles with respect to the tissue.

Purpose: To efficiently address uncertainty during inverse planning for HDR BT in order to robustly optimize the pose of the needles before insertion, that is, to facilitate path planning for robotic needle placement.

Methods: We use a form of stochastic linear programming to model the inverse treatment planning problem. To account for uncertainty, we consider random tissue displacements at the needle tip to simulate tissue deformation. Conventionally for stochastic linear programming, each simulated deformation is reflected by an addition to the linear programming problem which increases problem size and computational complexity substantially and leads to impractical runtime. We propose two efficient approaches for stochastic linear programming. First, we consider averaging dose coefficients to reduce the problem size. Second, we study weighting of the slack variables of an adjusted linear problem to approximate the full stochastic linear program. We compare different approaches to optimize the needle configurations and evaluate their robustness with respect to different amounts of tissue deformation.

Results: Our results illustrate that stochastic planning can improve the robustness of the treatment with respect to deformation. The proposed approaches approximating stochastic linear programming better conform to the tissue deformation compared to conventional linear programming. They show good correlation with the plans computed after deformation while reducing the runtime by two orders of magnitude compared to the complete stochastic linear program. Robust optimization of needle configurations takes on average 59.42 s. Skew needle configurations lead to mean coverage improvements compared to parallel needles from 0.39 to 2.94 percentage points, when 8 mm tissue deformation is considered. Considering tissue deformations from 4 to 10 mm during planning with weighted stochastic optimization and skew needles generally results in improved mean coverage from 1.77 to 4.21 percentage points.

Conclusions: We show that efficient stochastic optimization allows selecting needle configurations which are more robust with respect to potentially negative

effects of target deformation and displacement on the achievable prescription dose coverage. The approach facilitates robust path planning for robotic needle placement.

KEYWORDS
inverse optimization, robotic brachytherapy, robust optimization

1 | INTRODUCTION

In high-dose rate (HDR) prostate brachytherapy (BT), hollow needles are inserted into the target tissue. A radioactive source, usually Ir-192, is then inserted through the needles usually via an afterloader.[1] To determine the desired positions and dwell times of these sources, an optimization problem is solved in clinical practice.[2,3] Here, several competing clinical goals have to be considered, including sufficient dose in the clinical target volume (CTV) and sparing of surrounding organs at risk (OARs).

Multiple heuristic[4] and global[5–8] optimization methods have been proposed for optimizing source positions and dwell times. For prostate BT, optimization is often based on a transrectal ultrasound (TRUS) scan where the CTV, OARs, and inserted needles are reconstructed. The optimal position of the needles is often not part of the inverse planning problem in the current clinical workflow, where needles are first inserted and reconstructed and then the dwell times are optimized.[2]

Typically, an operator inserts needles manually. However, several robotic systems for needle insertion applications in BT have been proposed in recent years which promise increased needle placement accuracy.[9–13] Often, prostate implants rely on a template for needle placement. In contrast, robotic needle placement offers more flexibility since the needles can be inserted without a common template which potentially also allows for placement of skew needles. Skew needles increase the available variations for needle placement and have been shown to avoid critical structures, including the penile bulb, while reducing the number of needles and achieving plan quality superior or equal to the clinical plans.[14] However, the optimal needle configuration depends on the anatomy of the individual patient and is hard to predict beforehand.

Including the optimization of needle configurations in the inverse treatment planning problem has been proposed before.[14–19] However, a major unaddressed challenge in the context of prostate BT is the tissue deformation and displacement during the insertion which may influence the position and shape of the prostate and OARs.[20] Additionally, the deviation between the planned and actually inserted needle position can influence the dose distribution. While magnetic resonance imaging (MRI) or TRUS can be used to guide the needles more accurately, the problem of prostate deformation remains. Therefore, an additional TRUS or MRI scan after needle placement is often used to locate the needles and determine the shape and position of the prostate during treatment.[21,22] Then, the optimization of the source dwell times is based on the actual needle positions and the deformed and displaced prostate. However, the initially planned needle configuration is not necessarily robust to the deformation and displacement of the prostate or positioning errors of the needles.[23]

Uncertainty has rarely been studied in HDR-BT for inverse treatment optimization[3] but its impact on the treatment quality has been recognized.[24] Few approaches exist to account for uncertainty in the delineation in the inverse optimization problem utilizing min-max optimization.[25,26] Here, the optimization problem is extended by including several possible segmentations to increase the robustness of the solution to segmentation errors. However, the robustness of the needle configuration itself to CTV deformation is not considered.

We have previously studied stochastic optimization for uncertainty in needle placement and tissue deformation and implemented an approach in which we extended the original planning problem to consider deformed volumes.[27,28] While the results were promising, the runtime was infeasible for optimization of needle configurations.

In this work, we study the optimization of needle configurations considering the uncertainty of needle positioning and tissue deformation. We evaluate the robust needle configurations then by optimizing dwell times and source positions similar to the conventional approach. The proposed workflow for robust treatment plan optimization is shown in Figure 1. In essence, we propose more efficient versions of stochastic optimization and use it as a heuristic to identify robust needle configurations. We show that treatment quality improves when considering uncertainty with respect to tissue deformation and tissue displacement during the optimization of the needle configuration. Additionally, we study whether the flexibility of robotic needle positioning can improve treatment plan quality when considering uncertainty due to tissue deformation.

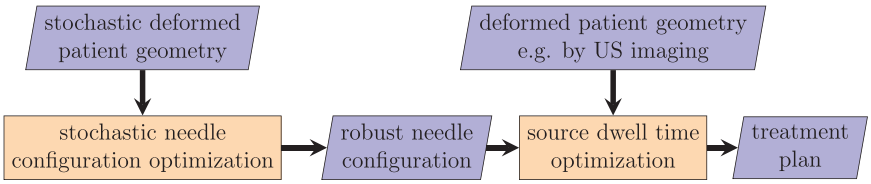

FIGURE 1 The proposed workflow for optimization of robust needle configuration and optimization of the final treatment plan. Stochastic uncertainty information is considered to find a robust needle configuration. Source dwell times are optimized considering imaged deformation and displacement after needle insertion.

2 | METHODS

2.1 | Inverse planning by linear optimization

We solve the inverse treatment planning problem for the static case by linear optimization. To represent the problem, the CTV and OARs (urethra and rectum) are discretized.

The linear optimization problem is set up with respect to a given needle configuration. Since there are no known optimal needle configurations, especially when considering the flexibility in position and orientation of robotic needle placement, we sample needle positions and orientations based on randomized heuristics. We model needles as straight line segments from the perineum to the basal part of the prostate. As a needle start point we sample a random point in the projection of the prostate on the axial slice through the perineum. The needle end point is a random point in the projection of the prostate on the axial slice through the basal part of the prostate. We introduce the *maximum lateral offset* to control the skewness of the needles. The lateral offset is the distance projected on the axial slice between the point in the perineum slice and the basal slice. A maximum lateral offset of zero results in parallel needles.

We only allow needles with a minimum distance of the needle radius from the urethra and other sampled needles. Note however, that the urethra is only contoured inside the prostate in our retrospective dataset. For puncture avoidance in a clinical application, the complete urethra needs to be contoured on all slices and needle implantation should be avoided anterior of the urethra. In our experiments we consider 18 gauge needles with possible source positions which are distributed equidistantly along the needle with a distance of 2 mm.

For each voxel i and source j, dose coefficients a_{ij} are calculated in the CTV and OARs for an HDR source of Ir-192, using the TG-43 formalism for a line source[29] in our in-house framework. These dose coefficients represent the dose delivered by a source to a specific voxel per dwell time of that source.

We set fixed upper bounds to dose in CTV and OARs and optimize the CTV coverage (V_{100}) by minimizing the slack representing the underdosage in the CTV. This leads to an optimization problem of the form

$$\min \sum_{s_i \in \mathbf{s}} s_i \tag{1}$$

$$\mathrm{A}\mathbf{x} + \mathbf{s} \geq \mathbf{b_l} \tag{2}$$

$$\mathrm{A}\mathbf{x} - \mathbf{s_u} \leq \mathbf{b_u} \tag{3}$$

$$s_i, s_{u,i} \geq 0, \quad \forall s_i, \forall s_{u,i} \tag{4}$$

$$\sum_{s_{u,i} \in \mathbf{s_u}} s_{u,i} \leq s_{sum} \tag{5}$$

$$x_j \leq d_{max}, \quad \forall x_j \tag{6}$$

$$\sum_{x_j \in \mathbf{x}} x_j \leq D_{max} \tag{7}$$

where A is the matrix of dose coefficients, $\mathbf{x}$ is the vector of dwell times, s_i are the entries of a vector $\mathbf{s}$ of slack variables measuring the deviation from the lower bound b_l on the dose for each voxel in the CTV. Similarly, the vector $\mathbf{s_u}$ describes the upper dose slack in all volumes of interest (VOIs). Furthermore, upper dose bounds $\mathbf{b_u}$, upper dwell time bounds d_{max}, and upper total dwell time D_{max} are restricted for the source dwell times x_j. Non-zero dwell times in the solution represent the set of active sources.

Since linear optimization results in the optimal solution with respect to the given constraints and needle configuration, we can directly compare the impact of different needle configurations on the plan quality. We refer to the linear problem with the undeformed CTV as **LP**. LP can be considered the reference approach as it assumes a perfect treatment geometry and neglects uncertainty.

In reality, this assumption often does not hold, and we therefore consider that source dwell times are computed for the deformed CTV after needle insertion, that is, when information is available about the actual deformation by needle insertion, for example, after US imaging. We construct the linear optimization problem similar to LP but based on the dose coefficients of the deformed CTV to compute the final treatment plan and the corresponding clinical metrics. We refer to this linear problem of the deformed CTV as **the deformed LP (DLP)**.

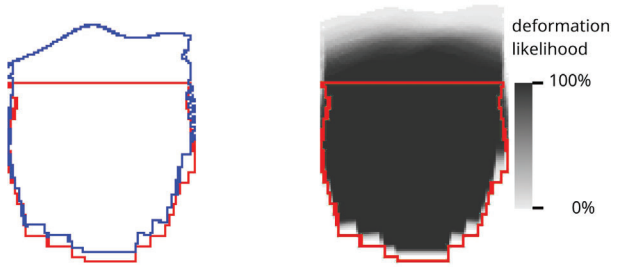

(a) single transformed CTV (b) multiple transformed CTVs (deformation likelihood)

FIGURE 2 Example coronal slice of a single transformed CTV (a) and a representation of multiple overlaid deformed CTVs (b), representing the deformation likelihood. Red indicates the contour of the original delineated CTV and blue the deformed CTV contour (a). The distribution of the deformed CTVs (b) is shown in shades of grey. Dark grey pixels correspond to a higher likelihood that the CTV is deformed to the respective position, lighter grey corresponds to a lower likelihood (b). CTV, clinical target volume.

2.2 | Uncertainty modeling

When inserting the needle, there is uncertainty with respect to the needle position relative to the tissue, mainly due to tissue deformation and tissue displacement. We model this uncertainty by creating randomly sampled deformations of the original volume. We define voxel correspondences, that is, voxels in the original volume that correspond to voxels in the deformed volume. Here, we use fix points at the border of the organ and shift voxels at the tip of the needle by adding an offset sampled from a constrained normal distribution along the needle trajectory. Using thin plate spline interpolation,[30] we shift all remaining voxels of the original volume to represent the deformation. This approach is similar to previous geometric models for deformation modeling.[31] We study deformations of different mean values and with different standard deviation of the constrained normal distribution. We overlay M deformations as shown in Figure 2 and call this representation the **deformation likelihood**. The values in the deformation likelihood correspond to the likelihood that a voxel belongs to the deformed volume.

2.3 | Optimization of needle configuration

We propose to create robust treatment plans by solving the inverse optimization problem for multiple candidate needle configurations as shown in Figure 3. First, we sample N needle configurations and compute the deformation likelihood for each configuration, respectively, as described before. We solve a stochastic inverse planning problem for each needle configuration by including the respective deformation likelihood with the needle configuration. The resulting objective value provides a heuristic for the quality and robustness of the needle configuration. We select the configuration with the best objective value as the best needle configuration and compare three different stochastic inverse planning approaches which we introduce in the following sections and illustrate in Figure 4.

2.3.1 | Stochastic linear program

One approach to implement stochastic inverse planning with linear optimization is to add rows to the matrix A and vectors s and b corresponding to each deformed volume in the deformation likelihood.[27] Thereby we create a stochastic linear program (**SLP**) with

$$\hat{A} = \begin{pmatrix} A_1 \\ \vdots \\ A_M \end{pmatrix}, \quad \mathbf{b_I} = \begin{pmatrix} \mathbf{b_{I,1}} \\ \vdots \\ \mathbf{b_{I,M}} \end{pmatrix}, \quad \mathbf{s} = \begin{pmatrix} \mathbf{s_1} \\ \vdots \\ \mathbf{s_M} \end{pmatrix} \tag{8}$$

for N deformed volumes where $A_1, \dots, A_N$ are the respective matrices of the dose coefficients, the vectors $\mathbf{b_{I,1}}, \dots, \mathbf{b_{I,N}}$ constrain the upper dose in the deformed volumes, and $\mathbf{s_1}, \dots, \mathbf{s_N}$ are the additional vectors of the slack variables. However, with this approach, the problem size increases proportional to the number of considered deformations. Since computational effort for solving linear optimization problems increases at least polynomially with problem size,[32] solving linear optimization problems quickly becomes impractical as the numbers of deformations increases. Computational effort is especially critical when the optimization problem needs to be solved multiple times to find robust needle configurations.

2.3.2 | Averaged stochastic linear program

Instead of extending A, **s**, and **b**, we can average the dose coefficients to create an averaged stochastic linear program (**ASLP**). Therefore, the entries of $\hat{A}$ are $\hat{a}_{v,n} = \frac{a_{v,n,1}+\dots+a_{v,n,M}}{M}$ for every voxel v, source n, and deformations $1, \dots, M$. For each voxel in the original volume we determine the dose coefficients for the same voxel in each deformed volume and calculate the average. Thereby, the resulting optimization problem is of the same size. However, this representation does not fully capture the goal of treatment planning since it does not lead to an optimization of the average coverage over many deformation fields but rather optimizes the average dose distribution. Therefore, it may not necessarily lead to adequate coverage for actual deformations optimized by DLP.

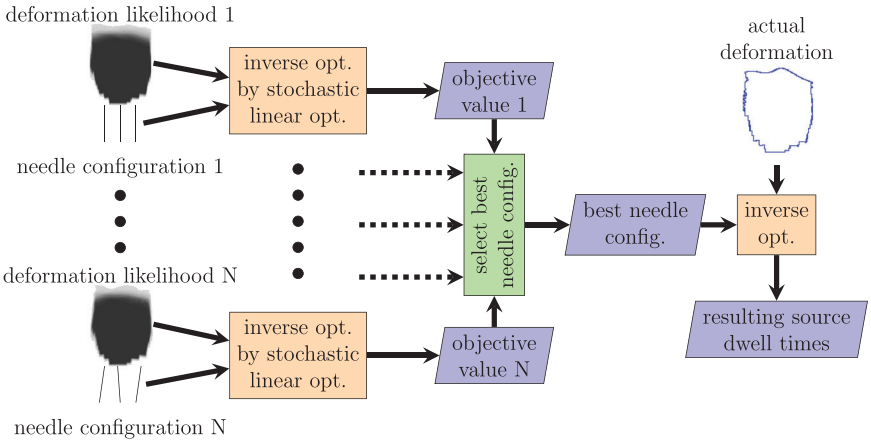

FIGURE 3 Flowchart of the needle optimization process. First, a needle configuration is identified which is robust to uncertainty of the CTV shape with respect to N randomized configurations by stochastic linear optimization considering uncertainty. Here, compare multiple approaches. Dotted lines indicate repeating blocks 2 to N-1. Second, the inverse problem is solved for the best needle configuration and a sampled deformation to determine the final source dwell times. CTV, clinical target volume.

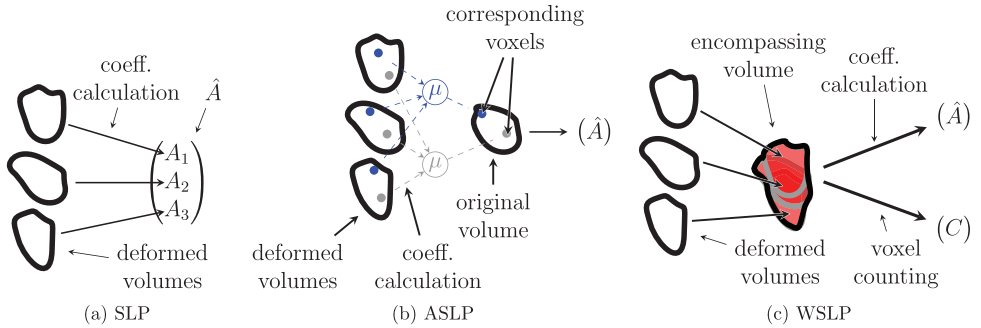

FIGURE 4 Illustration of the different stochastic optimization approaches for $M = 3$ deformations. In SLP (a), the new matrix of dose coefficients $\hat{A}$ is extended by dose coefficient matrices for every deformed volume. Note that the vectors of constraints and slack variable are also extended. In ASLP (b), entries of the new matrix $\hat{A}$ contain averaged values from corresponding voxel positions in deformed volumes. μ indicates the averaging operation. In WSLP (c), we calculate the new dose coefficient matrix $\hat{A}$ at voxel positions of the volume which encompasses all deformed volumes. An additional vector C counts the number of voxel occurrences. Darker red corresponds to a higher number of occurrences. ASLP, averaged stochastic linear program; SLP, stochastic linear program; WSLP, weighted stochastic linear program.

2.3.3 | Weighted stochastic linear program

We are not interested in optimizing the average dose in each voxel but in meeting the clinical goal of maximizing coverage and respecting dose constraints. When considering uncertainty, we try to fulfill these goals in the majority of expected scenarios. While SLP does approximate this goal well, SLP is computationally expensive. To address these issues, we introduce a weighted stochastic linear program (**WSLP**). Here, we discretize the positions which each deformed volume can occupy. For each considered deformation field, we count the number of voxels which fall into each cell of the discretized grid. We estimate the dose coefficients for each grid cell and optimize a linear problem of the from

$$\min \sum_{s_i \in \mathbf{s}} s_i \tag{9}$$

$$\hat{\mathbf{A}}\mathbf{x} + \mathbf{s} \geq \mathbf{b_l} \tag{10}$$

$$\hat{\mathbf{A}}\mathbf{x} - \mathbf{s_u} \leq \mathbf{b_u} \tag{11}$$

$$\sum_{s_{u,i} \in \mathbf{s_u}} s_{u,i} \leq s_{sum} \tag{12}$$

$$s_i, s_{u,i} \geq 0, \quad \forall s_i, \forall s_{u,i} \tag{13}$$

$$x_j \leq d_{max}, \quad \forall x_j \tag{14}$$

$$\sum_{x_j \in \mathbf{x}} x_j \leq D_{max} \tag{15}$$

where $\hat{\mathbf{A}}$ contains the dose coefficients of the grid cells. The vector $\mathbf{s}$ contains slack variables s_i for every grid cell of the CTV while the vector $\mathbf{s_u}$ contains slack variables $s_{u,i}$ for grid cells of all VOIs. The vector $\mathbf{s}$ is comprised of entries $\hat{s}_i = c_i \cdot s_i$. Here, $c_i = \frac{M}{\hat{c}_i}$, which describes the number of occurrences $\hat{c}_i$ of voxels in grid cell i relative to the number of deformation fields M. Similarly, entries of the vector $\mathbf{s_u}$ are $\hat{s}_{u,i} = c_i \cdot s_{u,i}$, where $s_{u,i}$ are entries in the upper dose slack vector $\mathbf{s_u}$.

The expression $c_i \cdot s_i$ incentivizes the optimizer to fulfill the lower dose bound $\mathbf{b_l}$ when $\hat{c}_i$ is large in the

TABLE 1 Delineated VOI sizes and average number of dose calculation points of the undeformed geometries of the patients (P1 to P5) in this study.

VOI	P1	P2	P3	P4	P5
Prostate	30.2 cm^3	26.7 cm^3	24.8 cm^3	44.3 cm^3	28.7 cm^3
Rectum	4.4 cm^3	3.4 cm^3	4.3 cm^3	6.3 cm^3	8.2 cm^3
Urethra	0.7 cm^3	0.8 cm^3	0.6 cm^3	1.1 cm^3	1.7 cm^3
Dose calc. points	2167	2147	1784	3341	2384

Note: We use needles of 200 mm length, 2 mm source tip offset and 2 mm source spacing for all experiments leading to 99 dwell positions per needle.

TABLE 2 Parameters of the constrained normal distributions which we use to sample deformation fields of the CTV.

Mean	Maximum
4 mm	6 mm
6 mm	10 mm
8 mm	14 mm
10 mm	18 mm

particular cell, that is, when the cell is part of the CTV in many deformations. In that case, slack is expensive because it is multiplied by $c_i \approx 1$. Therefore, the optimizer will prioritize the dose in the respective cell. When a cell is less populated, then $c_i >> 1$ and a small slack value can compensate large doses. The same logic applies to the upper dose slack $\mathbf{s_u}$.

2.4 | Patient data and experimental setup

In this retrospective study, we base our treatment planning evaluation on data from five patients previously treated with HDR-BT. Prostate (CTV) and bladder and rectum (OARs) are delineated by medical experts according to GEC-ESTRO recommendations without an additional margin to the prostate.[33] The VOI sizes are shown in Table 1.

We follow the dose prescriptions for HDR-BT boost according to the GEC-ESTRO guidelines.[33] We optimize for a prescribed CTV dose of 15 Gy in one fraction and set hard upper constraints on the dose in the rectum and urethra of 12.35 and 15 Gy, respectively. The upper constraint on the shell is tuned such that 95% coverage of the prescription dose in the CTV is achieved with 14 needles, that is $V_{100} = 95\%$.

We evaluate different CTV deformation magnitudes shown in Table 2 in the range of previously reported values.[20] For ASLP and WSLP, we create deformation likelihoods by sampling $M = 1000$ deformations compared to $M = 100$ deformations for SLP due to computational practicability.

We additionally compare the results after DLP for all approaches, that is, the optimal treatment plan for the optimized needle configuration and the deformed CTV. We study different numbers of needles, and average the results from experiments with 10 different deformed CTVs for DLP to improve statistical robustness of the results. Note that we use different random seeds to deform the CTV for DLP than we use to generate the deformation likelihood. We sample $N = 100$ randomized needle configurations to find the most robust configuration for the respective deformation according to the different approaches. For significance tests we use the student's *t*-test and report the significance for *p*-values ≤ 0.01.

3 | RESULTS

3.1 | Coverage without DLP

First, we evaluate the coverage after the stochastic optimization without adapting the source weights to the actual deformation. The source weights are optimal with respect to the stochastic optimization problem while coverage is evaluated and averaged for 100 deformed volumes. Thereby, we analyze how much information about the deformation is represented in the stochastic optimization approaches. Figure 5 shows the resulting coverage for all patients and 100 different needle configurations for increasing mean deformation. Coverage decreases for increasing mean deformation. Note that 95% is achieved when deformation is not considered. On average the source weights determined by the stochastic optimization approaches can better maintain the coverage especially for larger deformations. Differences of LP compared to the stochastic approaches are statistically significant with $p < 10^{-6}$ for all mean deformations except for the difference between LP and ASLP for 4 mm mean deformation where $p = 0.021$.

3.2 | Correlation to DLP objective values

Additionally, we evaluate how well the stochastic optimization correlates with the final optimization value of DLP, that is, the final treatment plan. Thereby, we

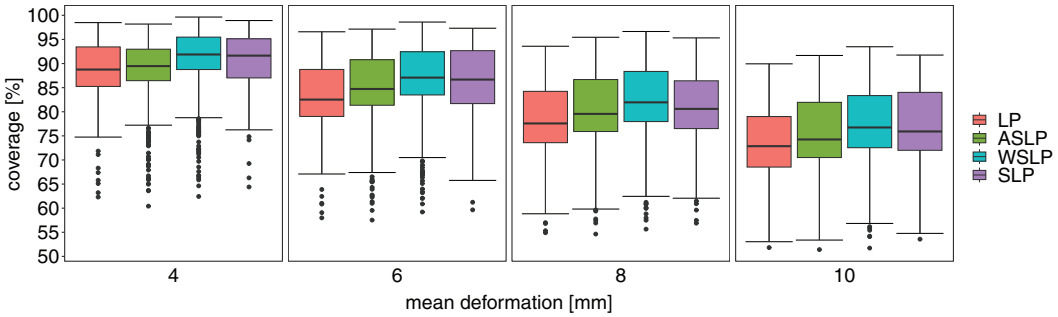

FIGURE 5 Boxplots of the coverage of the CTV without DLP for 14 needles and increasing amount of deformation. Shown are the resulting coverage for all needle configurations where source weights are optimized by the respective approach. CTV, clinical target volume.

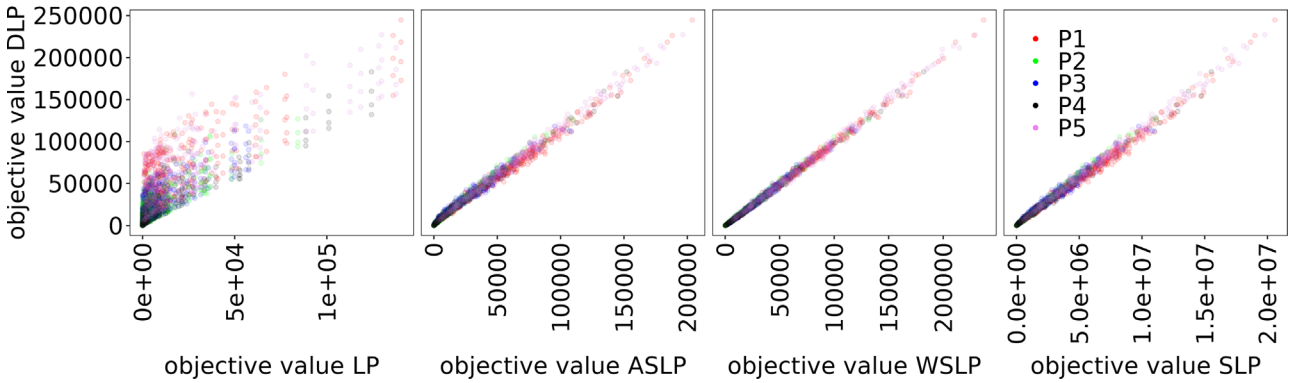

FIGURE 6 Scatter plots of corresponding objective value of the stochastic optimization and objective value for the deformed CTV after sampling for all experiments, optimization methods, and patients P1, …, P5. ASLP and WSLP objective values are calculated with a deformation likelihood composed of $M = 1000$ deformations while SLP includes $M = 100$ deformations. ASLP, averaged stochastic linear program; CTV, clinical target volume; SLP, stochastic linear program; WSLP, weighted stochastic linear program.

analyze whether we can use the stochastic optimization as heuristics to search for robust needle configurations. In Figure 6 we show scatter plots of the resulting objective values. The plots show the relationship between the stochastic optimization and the final optimization after sampling particular deformations. When we compare the objective values of LP with the DLP objective values, we see less correlation with respect to the spearman correlation (0.92 ± 0.05) compared to the ASLP objective value (0.96 ± 0.02), WSLP objective value (0.99 ± 0.01), and SLP objective value (0.98 ± 0.01). Here, we calculate the correlation for each patient, mean deformation, and number of optimization samples individually and average the results. Additionally, the standard deviation is indicated. Differences between LP correlation and all stochastic approaches are significant with $p \leq 10^{-12}$. Differences between ASLP and the other stochastic optimization approaches are also significant with $p \leq 10^{-6}$. WSLP and SLP are not significantly different with $p = 0.065$.

3.3 | Runtime comparison

In this work, we propose to search for an optimal needle position by evaluating randomized candidate configurations. Therefore, the stochastic optimization needs to be calculated for every candidate configuration. We evaluate the runtime on an AMD Ryzen 9 3950X CPU. Considering the runtime difference in Figure 7, where an optimization of SLP including dose coefficient calculation takes on average 36.92 min compared to 17.27 s for WSLP, we evaluate the search only for LP, ASLP, and WSLP. An end to end optimization

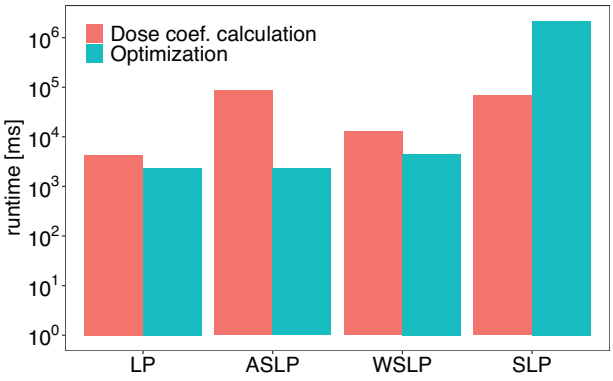

FIGURE 7 Average runtime of the studied approaches for inverse optimization. The runtime is split up in dose coefficient calculation and optimization of the resulting problem. Note the logarithmic scale on the *y*-axis.

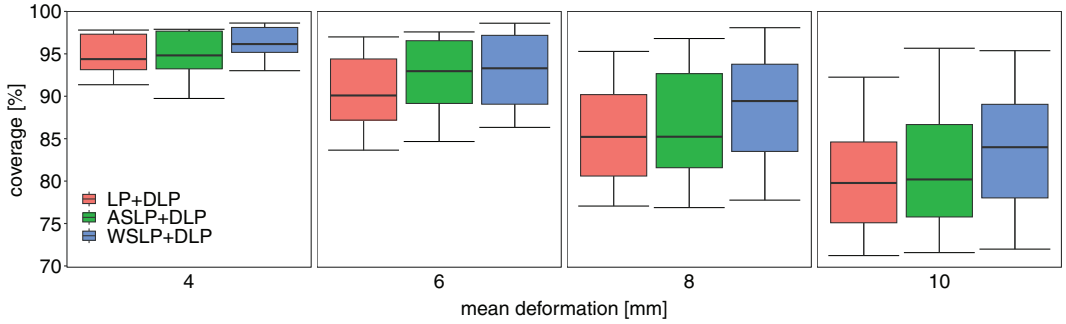

FIGURE 8 Boxplots of the coverage of the CTV for 14 needles and increasing mean deformation. Needle configurations are optimized with the respective stochastic approaches. Dwell times are optimized with DLP. CTV, clinical target volume.

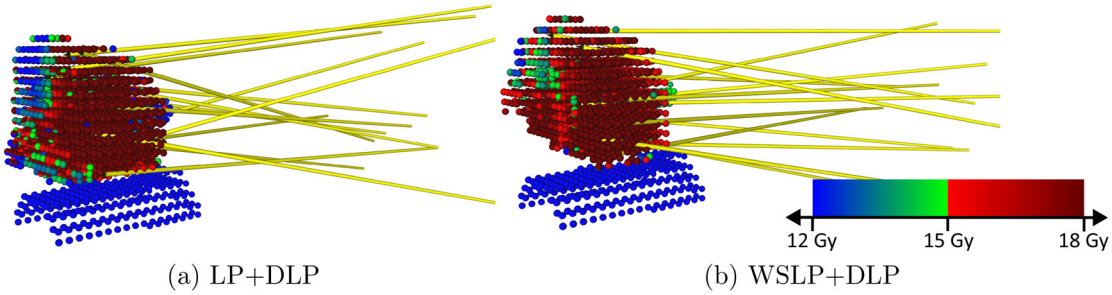

FIGURE 9 3D dose comparison for the optimal needle configuration with respect to LP optimization (a) and WSLP (b). Dwell times are optimized with DLP in both cases. Needles in yellow; voxel color corresponds to the dose with higher dose in red. WSLP, weighted stochastic linear program.

with 100 candidate needle configurations takes on average 59.42 s with WSLP when using distributed computing with 100 parallel optimizations on four machines.

3.4 | Coverage results with DLP

Figure 8 shows the resulting coverage after the search for the optimal needle configuration for the respective stochastic approaches. Note, that the final dwell time optimization is computed for sampled deformations, that is each computed treatment plan is optimal with respect to the needle configuration. We show here how the magnitude of deformation affects the coverage. While needle selection with ASLP and WSLP still improves the coverage compared to LP, large deformation of the CTV decreases mean coverage to 80.44% and 83.99% for ASLP+DLP and WSLP+DLP, respectively at 10 mm mean deformation. While coverage with ASLP+DLP is only significantly better for 6 mm mean deformation ($p = 0.009$), WSLP+DLP is significantly better than LP+DLP for all tested mean deformations ($p \leq 0.01$). The mean OAR dose volume constraints including D_{2cc} of the rectum (8.24 Gy, 8.21 Gy, and 8.14 Gy for LP+DLP, ASLP+DLP, and WSLP+DLP), D_{10} of the urethra (14.77 Gy, 14.70 Gy, and 14.74 Gy for LP+DLP, ASLP+DLP, and WSLP+DLP), and D_{30} (14.08 Gy, 14.03 Gy, and 14.10 Gy for LP+DLP, ASLP+DLP, and WSLP+DLP) are within GEC-ESTRO recommendations.[33] Additionally, Figure S1 shows similar results for an increasing number of needles.

An example of the difference in the resulting 3D dose distribution is shown in Figure 9 and the DVH for this case in Figure S2. The two needle configurations cause a difference in deformation. The resulting inverse optimization problem leads to a higher coverage of the prostate for the needle configuration resulting from the WSLP-based search.

In Figure 10 we show the impact of increasing needle skewness in the candidate needle configurations. Here, the lateral offset controls the maximal skewness of the needles. It is the upper limit of the distance from the needle tip to the needle rear end in the axial slice. Note that we add additional candidate needle configurations with larger skewness to the original candidate needle configurations. Therefore, needle configurations with larger lateral offset also contain needle configurations with lower lateral offset. Generally, higher needle skewness allows for a larger improvement in coverage of WSLP+DLP over LP+DLP optimized needle configurations. This improvement is even larger for increasing number of needles up to a mean improvement in coverage of 3.44 percentage points for 14 needles and 12 mm skewness compared to 1.33 percentage points for 0 mm skewness. Note, that the coverage also improves with

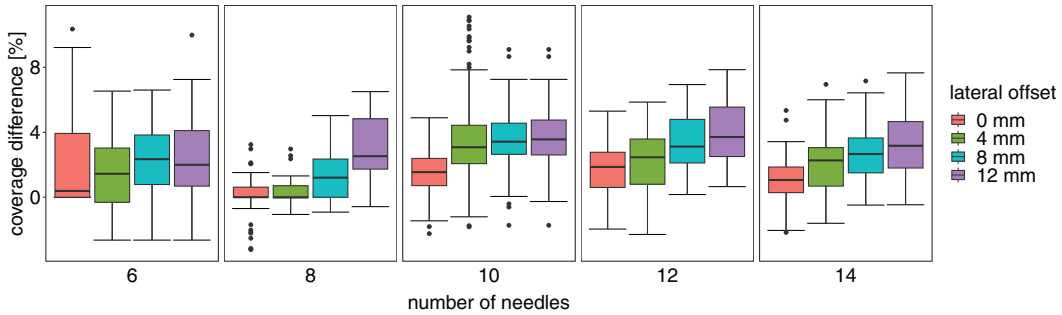

FIGURE 10 Boxplots of optimized CTV coverage difference for 8 mm mean deformation and WSLP+DLP compared to LP+DLP. Shown is the impact of the maximum sampled needle lateral offset, that is maximum needle skewness, for different numbers of needles. CTV, clinical target volume; WSLP, weighted stochastic linear program.

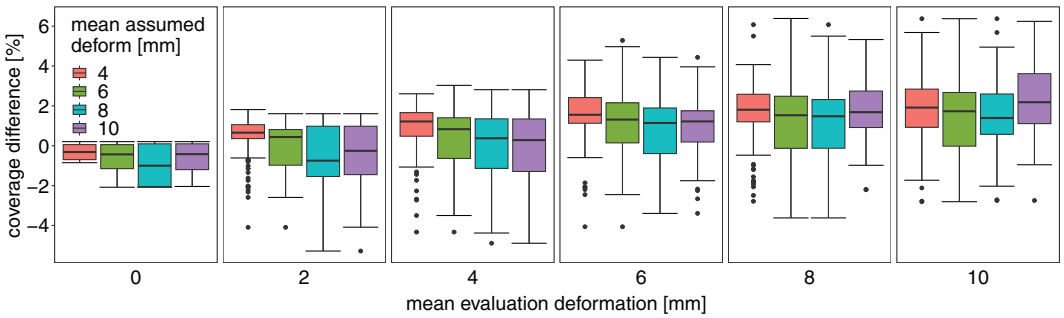

FIGURE 11 Boxplots of optimized CTV coverage difference of 14 needles and WSLP+DLP compared to LP+DLP. Shown is the impact of a difference in assumed mean deformatio3n and the actual mean deformation. CTV, clinical target volume; WSLP, weighted stochastic linear program.

skewed needles for the undeformed target as shown in Figure S3.

Figure 11 shows how a mismatch of assumed deformation and actually observed deformation affects our approach. Here, the parameters of the stochastic uncertainty we use to optimize the needle configurations differ from the deformation for DLP. While the improvement in coverage is generally larger when assumed mean and evaluated mean deformation are similar, small differences only show a small degradation in the coverage improvement. A decrease in coverage only occurs for small evaluated deformation and large assumed deformation.

4 | DISCUSSION

As our first result, Figure 5 confirms the clinical practice and shows that optimizing dwell times on the actual patient geometry after needle insertion is sensible when considering even relatively small deformation. The coverage can increase above the 95% which was planned on the static geometry due to occasional favourable deformations. However, in the majority of cases the coverage decreases by over 10 percentage points. While the stochastic approaches improve coverage over LP and thereby show that relevant information is captured in the stochastic optimization problems, the dwell times need to be optimized for the actual patient geometry after the selection and placement of the optimal needle configuration.

Considering Figure 6, we show that SLP, ASLP, and WSLP are good heuristics for predicting the quality and robustness of needle configurations when introducing CTV deformation. WSLP shows the strongest correlation indicating that it can best approximate the problem of maximizing the average coverage compared to ASLP which approximates the maximization of the average dose distribution.

As shown in Figure 7, the runtime of SLP makes its use for the optimization of needle configuration infeasible. ASLP and WSLP only add a small additional runtime to the reference inverse optimization. ASLP requires more runtime than WSLP since the dose coefficients need to be calculated for every deformation, whereas WSLP only calculates the dose coefficients on the discretization grid. The slightly larger optimization problem of WSLP has a smaller impact on the runtime in our experiments. A comparison to other methods is difficult due to the different hardware and different problem sizes (dose calculation points and dwell positions). Still, our approach for inverse optimization is in the range of the previously published IPIP optimization which had an average runtime of 30.1 s.[34] Furthermore, needle

optimization can easily be parallelized which profits from modern hardware.

Applying the proposed heuristics to a needle configuration search, Figure 8 shows that the coverage can be improved compared to an LP guided search which does not consider deformation uncertainty. Note that we mainly show the coverage results here, since we optimize for coverage by solving a linear optimization problem with the same hard upper dose constraints for the VOIs for all experiments with the same patient. This allows us to directly compare plan quality by comparing coverage, while other clinical dose indices remain similar due to the hard constraints.

Results for coverage show that needle configurations which are optimal when deformation is not considered can be suboptimal when deformation is considered. In our experiments, larger deformation generally reduces the coverage also for ASLP and WSLP optimized needle configurations. Larger deformations usually caused the prostate to move away from the needle tips which reduced achievable coverage. Since the needle position is commonly adjusted during image guided insertion, this could be avoided. If this behavior is modeled in our simulation, our approach could still be applied to search for the optimal needle configuration.

Considering Figure 10, we have shown that skew needles can further improve the coverage in stochastic optimization, which are not necessarily intuitive considering Figure 9. The improvement of WSLP+DLP in general and larger lateral offset in particular increases with increasing needles count due to larger deformations and displacements of the CTV with a larger number of needles. The original CTV shows less overlap with the deformed CTVs for a larger number of needles, leading to the increased improvement with WSLP+DLP over LP+DLP.

In practice, predicting the correct stochastic deformation is challenging. However, Figure 11 indicates that small differences in the assumed deformation compared to the actual deformation only lead to small degradation in coverage. Still, correctly predicting the stochastic deformation will lead to optimal results with the presented approach. In general, several factors impact the treatment quality including several dosimetric indices and other clinical goals, for example, the number of needles. Our approach could lead to reduced margins, reduced numbers of needles, and increased dosimetric indices due to more robust needle configurations. The clinical workflow we propose would start with a 3D scan, for example CT, MRI, or potentially TRUS, and contouring of the relevant VOIs. Based on this image data, the needle configuration is optimized. Subsequently, the treatment continues similar to the current workflow by TRUS guided (robotic) needle insertion and dwell time optimization.

There are several limitations of our results. First, we evaluated our approach on a small number of patients. Nevertheless, we showed significant improvements in coverage for the stochastic approaches over the non-stochastic approach. In this study, we use a simple model to simulate deformation with stochastic uncertainty. Several previous works have studied the interaction of tissue and needles during needle insertion.[35–37] These methods are often model based, for example geometry based models or finite element method (FEM) simulations, or they are data driven including machine learning methods. Our approach for deformation simulation is geometry based which does not necessarily resemble the exact physical tissue parameters. Note however, that obtaining exact tissue properties is typically difficult and that current physical models do not yet reflect the full complexity of needle-tissue interaction. Moreover, our purpose is to increase robustness to possible deformations, independently of their physical cause. A simple model resulting in a large shape variation may therefore be preferable for robust planning. Still, our results should be validated with more sophisticated deformation models which better resemble the clinical data. Note that the method can be adapted to different deformation models.

Robustness of the treatment plan is commonly addressed by adding additional margins to the CTV. However, the deformation depends on the needle configuration and is hard to accurately predict. When deciding for a fixed margin there is a trade-off between increased toxicity in normal tissue and insufficient dose coverage in the CTV. In contrast, our approach finds an optimal solution with respect to the expected deformation.

Our approach for the optimization the needle configuration is a random search with a heuristic based on stochastic linear optimization. Other heuristic optimization methods including simulated annealing for the optimization of needle configurations[38] can be extended by our heuristic to improve the robustness of the optimized needle configurations.

5 | CONCLUSION

Tissue deformation presents a challenge when planning optimal needle configurations. We apply and compare different approaches for stochastic linear planning to compute a heuristic for the robustness and quality of candidate needle configurations. We show that the needle configurations can be computed quickly and lead to good plan quality when deformations occur. We illustrate how the proposed approach can be used to search for optimal needle configurations which are robust to CTV deformation and improve the CTV coverage.

ACKNOWLEDGMENTS

This work was partially funded by Deutsche Forschungsgemeinschaft (grant SCHL 1844/6-1).

Open access funding enabled and organized by Projekt DEAL.

CONFLICT OF INTEREST STATEMENT

The authors declare that they have no conflict of interest.

INFORMED CONSENT

For this type of study informed consent is not required.

REFERENCES

1. Li Y, Yang C, Bahl A, Persad R, Melhuish C. A review on the techniques used in prostate brachytherapy. *Cogn Comput Syst*. 2022;4:317-328.
2. Demanes DJ, Ghilezan MI. High-dose-rate brachytherapy as monotherapy for prostate cancer. *Brachytherapy*. 2014;13:529-541.
3. de Boeck L, Beliën J, Egyed W. Dose optimization in high-dose-rate brachytherapy: a literature review of quantitative models from 1990 to 2010. *Oper Res Health Care*. 2014;3:80-90.
4. Lessard E, Pouliot J. Inverse planning anatomy-based dose optimization for HDR-brachytherapy of the prostate using fast simulated annealing algorithm and dedicated objective function. *Med Phys*. 2001;28:773-779.
5. Bélanger C, Cui S, Ma Y, Després P, Adam M Cunha J, Beaulieu L. A GPU-based multi-criteria optimization algorithm for HDR brachytherapy. *Phys Med Biol*. 2019;64:105005.
6. Antaki M, Deufel CL, Enger SA. Fast mixed integer optimization (FMIO) for high dose rate brachytherapy. *Phys Med Biol*. 2020;65:215005.
7. Breedveld S, Bennan ABA, Aluwini S, Schaart DR, Kolkman-Deurloo I-KK, Heijmen BJM. Fast automated multi-criteria planning for HDR brachytherapy explored for prostate cancer. *Phys Med Biol*. 2019;64:205002.
8. Morén B, Larsson T, Carlsson Tedgren Å. Mathematical optimization of high dose-rate brachytherapy-derivation of a linear penalty model from a dose-volume model. *Phys Med Biol*. 2018;63:065011.
9. Aleong AM, Looi T, Luo K, et al. Preliminary study of a modular MR-compatible robot for image-guided insertion of multiple needles. *Front Oncol*. 2022;12:829369.
10. Tucan P, Vaida C, Horvath D, et al. Design and experimental setup of a robotic medical instrument for brachytherapy in non-resectable liver tumors. *Cancers*. 2022;14:5841.
11. Lin X, Zhou S, Wen T, Jiang S, Wang C, Chen J. A novel multi-DoF surgical robotic system for brachytherapy on liver tumor: design and control. *Int J Comput Assist Radiol Surg*. 2021;16:1003-1014.
12. Adams Q, Hopfensperger KM, Kim Y, Wu X, Flynn RT. 169 Yb-based rotating shield brachytherapy for prostate cancer. *Med Phys*. 2020;47:6430-6439.
13. Garg A, Siauw T, Berenson D, et al. Robot-guided open-loop insertion of skew-line needle arrangements for high dose rate brachytherapy. *IEEE Trans Automat Sci Eng*. 2013;10:948-956.
14. Siauw T, Cunha A, Berenson D, et al. NPIP: a skew line needle configuration optimization system for HDR brachytherapy. *Med Phys*. 2012;39:4339-4346.
15. Aumüller P, Rothfuss A, Polednik M, et al. Multiple direction needle-path planning and inverse dose optimization for robotic low-dose rate brachytherapy. *Z fur Med Phys*. 2022;32:173-187.
16. Chatigny PY, Bélanger C, Poulin É, Beaulieu L. Catheters and dose optimization using a modified CVT algorithm and multi-criteria optimization in prostate HDR brachytherapy. *Med Phys*. 2022;49:6575-6587.
17. Wang C, Gonzalez Y, Shen C, Hrycushko B, Jia X. Simultaneous needle catheter selection and dwell time optimization for preplanning of high-dose-rate brachytherapy of prostate cancer. *Phys Med Biol*. 2021;66:055028.
18. Borot de Battisti M, Maenhout M, Denis de Senneville B, et al. An automated optimization tool for high-dose-rate (HDR) prostate brachytherapy with divergent needle pattern. *Phys Med Biol*. 2015;60:7567-7583.
19. Guthier CV, Damato AL, Hesser JW, Viswanathan AN, Cormack RA. A fast inverse treatment planning strategy facilitating optimized catheter selection in image-guided high-dose-rate interstitial gynecologic brachytherapy. *Med Phys*. 2017;44:6117-6127.
20. Stone NN, Roy J, Hong S, Lo Y-C, Stock RG. Prostate gland motion and deformation caused by needle placement during brachytherapy. *Brachytherapy*. 2002;1:154-160.
21. Crook J, Marbán M, Batchelar D. HDR prostate brachytherapy. *Semin Radiat Oncol*. 2020;30:49-60.
22. Wang J, Tanderup K, Cunha A, et al. Magnetic resonance imaging basics for the prostate brachytherapist. *Brachytherapy*. 2017;16:715-727.
23. Poder J, Koprivec D, Dookie Y, et al. HDR prostate brachytherapy plan robustness and its effect on in-vivo source tracking error thresholds: a multi-institutional study. *Med Phys*. 2022;49:3529-3537.
24. Kirisits C, Rivard MJ, Baltas D, et al. Review of clinical brachytherapy uncertainties: analysis guidelines of GEC-ESTRO and the AAPM. *Radiother Oncol*. 2014;110:199-212.
25. Balvert M, den Hertog D, Hoffmann AL. Robust optimization of dose-volume metrics for prostate HDR-brachytherapy incorporating target and OAR volume delineation uncertainties. *INFORMS J Comput*. 2019;31:100-114.
26. van der Meer MC, Bosman PAN, Niatsetski Y, Alderliesten T, Pieters BR, Bel A. Robust optimization for HDR prostate brachytherapy applied to organ reconstruction uncertainty. *Phys Med Biol*. 2021;66:055001.
27. Yu T, Siebert F-A, Schlaefer A. A stochastic optimization approach accounting for uncertainty in HDR brachytherapy needle Placement. *Int J Comp Assist Radiol Surg*. 2018;13:34-35.
28. Gerlach S, Siebert F, Schlaefer A. BReP-SNAP-T-54: Efficient stochastic optimization accounting for uncertainty in HDR prostate brachytherapy needle placement. *Med Phys*. 2020;47:e458.
29. Rivard MJ, Coursey BM, DeWerd LA, et al. Update of AAPM Task Group No. 43 Report: a revised AAPM protocol for brachytherapy dose calculations. *Med Phys*. 2004;31:633-674.
30. Davis MH, Khotanzad A, Flamig DP, Harms SE. A physics-based coordinate transformation for 3-D image matching. *IEEE Trans Med Imaging*. 1997;16:317-328.
31. Cover SA, Ezquerra NF, O'Brien JF, Rowe R, Gadacz T, Palm E. Interactively deformable models for surgery simulation. *IEEE Comput Graph Appl*. 1993;13:68-75.
32. Vanderbei RJ. *Linear Programming: Foundations and Extensions*. Springer; 2020.
33. Henry A, Pieters BR, André Siebert F, Hoskin P. GEC-ESTRO ACROP prostate brachytherapy guidelines. *Radiother Oncol*. 2022;167:244-251.
34. Siauw T, Cunha A, Atamtürk A, Hsu I-C, Pouliot J, Goldberg K. IPIP: a new approach to inverse planning for HDR brachytherapy by directly optimizing dosimetric indices. *Med Phys*. 2011;38:4045-4051.
35. Afshar M, Carriere J, Rouhani H, et al. Accurate tissue deformation modeling using a kalman filter and ADMM-based projective dynamics. *IEEE/ASME Trans Mechatron*. 2022;27:2194-2203.
36. Liang D, Jiang S, Yang Z, Wang X. Simulation and experiment of soft-tissue deformation in prostate brachytherapy. *Proc Inst Mech Eng B: J Eng Manuf*. 2016;230:532-544.
37. Zhang J, Zhong Y, Gu C. Deformable models for surgical simulation: a survey. *IEEE Rev Biomed Eng*. 2018;11:143-164.
38. Karabis A, Giannouli S, Baltas D. HIPO: A hybrid inverse treatment planning optimization algorithm in HDR brachytherapy. *Radiother Oncol*. 2005;76(Suppl 2):S29.

SUPPORTING INFORMATION

Additional supporting information can be found online in the Supporting Information section at the end of this article.

How to cite this article: Gerlach S, Siebert F-A, Schlaefer A. Robust stochastic optimization of needle configurations for robotic HDR prostate brachytherapy. *Med Phys*. 2023;1-12. https://doi.org/10.1002/mp.16804